Published October 7, 2013

These evidences indicate that different Ub-linkages could be part of the Ub-coat on the invading *Salmonella*. Further, we showed that autophagic machinery targeting did not depend solely on K63- or linear-Ub linkages (Fig. S2, B and C). These results suggest that autophagic machinery could target different Ub linkages, or other linkages besides K63 and linear might be specifically favored by autophagic machinery.

Atg16L1 directly interacts with ubiquitin and FIP200 through the WD β-propellers and residues 239–242, respectively (Figs. 3–5). The WD β-propellers of Atg16L1 are required to localize the Atg16L1 complex and LC3 to ubiquitinated substrates in the absence of FIP200 (Fig. 4, E–L). This result explains our previous observation that LC3 localized to a single membrane in *Salmonella*-infected FIP200-KO cells (Kageyama et al., 2011). Because the WD β-propellers have an affinity for Ub (Fig. 3) and host cellular proteins are ubiquitinated upon bacterial invasion (Fig. 1 and Fig. S1), PE conjugation of LC3 could occur in Ub-positive endosomal membranes in FIP200-KO cells. We do not have a clear answer as to why Atg16L1 has dual (or triple) recruiting mechanisms. It is noteworthy that Atg16 in simple eukaryote-like budding yeast lacks the WD β-propellers. One interesting possibility is that higher eukaryotes such as mammals have evolved to use autophagy to clear invading pathogens, and to secure such a complex process Atg16L1 may be involved in a back-up system. Interestingly, the WD β-propellers also seem to be involved in starvation-induced autophagy. p62-positive foci are observed at the autophagosome formation site (Itakura and Mizushima, 2010). We also observed Ub-positive signals at the starvation-induced autophagosome formation site (unpublished data). Thus, mammals may be evolved to use the Ub-binding capacity of Atg16L1 in starvation-induced autophagy.

A combination of Atg16L1 239–242A and ΔWD mutations severely impaired starvation-induced autophagy (Fig. S5), while selective autophagy against invading pathogens still occurred (Fig. 6; and Fig. S5, C–F). This indicates that interactions between Atg16L1 and FIP200 or Ub are not sufficient to localize the Atg16L1 complex in selective autophagy. We identified other important amino acids, 194–195 in Atg16L1 (Fig. 6 and Fig. S5). Because the ΔWD, 239–242A, and 194–195A mutations synergistically reduced the recruitment of Atg16L1 to the substrate (Fig. 6 and Fig. S5), we propose that all of these regions help localize the Atg16L1 complex to the ubiquitinated substrate (Fig. 7). Because residues 194–195 of Atg16L1 do not appear to be involved in FIP200 binding, Atg16L1 dimerization, or interactions with other Atg proteins (unpublished data), the region could interact with an unidentified factor. Interestingly, the Atg16L1 ΔWD construct contains the 194–195 region, although expression of the ΔWD mutant severely blocked LC3 recruitment in FIP200-KO cells (Fig. 4, J and L). The absence of a double membrane in these cells may lead to loss of the interaction partner for the 194–195 region, although we do not know the target(s) of this region.

In this study, we have uncovered the mechanisms by which selective autophagy responds to invading pathogens and shown that ubiquitinated substrates are recognized by the Atg16L1 complex independently of an LC3-mediated mechanism. These discoveries are similar to another Ub-mediated endosomal process, the multi-vesicular body pathway. Cargo proteins are ubiquitinated and the molecular machinery involved in this pathway, called ESCRT, is recruited by directly binding to Ub (Katzmann et al., 2001). Furthermore, our model may be applicable to Parkin-mediated autophagy against mitochondria, in which mitochondria are also decorated with Ub (Youle and Narendra, 2011). Thus, we provide a novel role for Ub among its many diverse functions. Our findings will open up new avenues in the study of autophagy.

Materials and methods

Reagents and antibodies

Cell culture reagents were purchased from Invitrogen. The following antibodies were used: anti–mouse Atg16L1 (Mizushima et al., 2003), anti-p62 (MBL), anti-LC3 (MBL), anti-transferrin receptor (Invitrogen), anti-poly Ub (clone FK2; BIOMOL), anti-K48 linked Ub (clone Apu2; EMD Millipore), anti-K63 linked Ub (clone Apu3; EMD Millipore) anti-galectin3 (Santa Cruz Biotechnology, Inc.), anti-Lamp1 (Santa Cruz Biotechnology, Inc.), anti-FLAG (clone M2; Sigma-Aldrich), anti-GFP (Roche), anti-Myc (clone 9E10), and anti–α-tubulin (clone B5-1-2; Sigma-Aldrich). All other reagents were purchased from Sigma-Aldrich.

DNA engineering and recombinant retroviruses

The pMRX-IRES-puro and pMRX-IRES-blast vectors were gifts from S. Yamaoka (Tokyo Medical and Dental University, Tokyo, Japan; Saitoh et al., 2003). To generate recombinant retroviruses, cDNAs corresponding to mStrawberry (mStr)-tagged galectin3, mStr-Ub, GFP-Ub, and GFP-p62 were subcloned into the pMRX-IRES-puro vector. Various human Atg16L1β (isoform-1) mutants were cloned into the pMRX vector, including full-length (1–607), ΔWD repeat domain (1–249), and the Crohn's disease–associated mutant (T300A; Fujita et al., 2009). In addition, pMRX constructs were generated to encode various GFP-tagged Atg proteins, including LC3 (N terminus), Atg5 (N terminus), WIPI1 (N terminus), Atg14L (N terminus), Atg9L1 (C terminus), and ULK1 (C terminus; Kageyama et al., 2011), as previously reported. Recombinant retroviruses were prepared as previously described (Saitoh et al., 2003). To prepare recombinant proteins, cDNA corresponding to Ub was subcloned into the pGEX6P-1 vector, and cDNA corresponding to FLAG-tagged wild-type or the Crohn's disease–associated mutant of the WD β-propellers of Atg16L1 was subcloned into the pCold-TF vector (Takara Bio Inc.).

Cell culture and retroviral infections

Plat-E cells were provided by T. Kitamura (The University of Tokyo, Tokyo, Japan; Morita et al., 2000). HeLa cells, HEK293T cells, NIH3T3 cells, wild-type MEFs, and autophagy-deficient MEFs (Atg5-KO, Atg14L-KO, Atg9L1-KO, Atg16L1-Δ/Δ, and FIP200-KO) were grown in DMEM supplemented with 10% fetal bovine serum, 2 mM L-glutamine, 5 U/ml penicillin, and 50 U/ml streptomycin in a 5% CO_2 incubator at 37°C (Kuma et al., 2004; Fujita et al., 2008a; Saitoh et al., 2008, 2009; Hara and Mizushima, 2009; Matsunaga et al., 2009; Nishimura et al., 2013). Stable transformants were selected in growth medium with 1 μg/ml puromycin or 5 μg/ml blasticidin (Invivogen).

Western blotting

Samples were subjected to SDS-PAGE, and transferred to polyvinylidene fluoride membranes. The membranes were blocked with TBST (TBS and 0.1% Tween 20) containing 1% skim milk and were then incubated overnight at 4°C with primary antibodies 1,000–3,000× diluted in the blocking solution. Membranes were washed three times with TBST, incubated for 1 h at room temperature with 10,000× dilutions of HRP-conjugated secondary antibodies (GE Healthcare) in the blocking solution, and washed five times with TBST. Immunoreactive bands were then detected using ECL plus (GE Healthcare) and a chemiluminescence detector (LAS-3000, Fujifilm; Kimura et al., 2009).

Bacterial infections and bead transfections

Salmonella enterica serovar Typhimurium (SR-11 x3181) was provided by the Research Institute of Microbial Disease, Osaka University (Osaka, Japan). Bacteria were grown overnight at 37°C, and then sub-cultured at

Published October 7, 2013

1:33 for 3 h in LB without antibiotics. The bacterial inocula were prepared by pelleting at 10,000 *g* for 2 min, and were then added to host cells at a multiplicity of infection (MOI) of 10–100 at 37°C with 5% CO_2 (Kageyama et al., 2011). Bead transfections were performed as previously reported (Kobayashi et al., 2010). Transfection reagent-coated beads were prepared by mixing the beads (NH_2-, 17145–5; PolySciences, Inc.) with Effectene transfection reagent (301425; QIAGEN), according to the manufacturer's instructions except that bead suspension was used instead of DNA solution. The resulting bead mixture (~100 µl) was further mixed with 1 ml of growth medium, and added to cells by replacing the medium. After incubation with the bead mixture for 1 h at 37°C in a CO_2 incubator, the cells were washed twice with fresh growth medium to remove unattached beads, and further incubated for the time indicated in each experiment.

Immunofluorescence and microscopy

Cells were cultured on coverslips, fixed with 3% PFA in PBS for 10 min, and permeabilized with 50 µg/ ml digitonin in PBS for 5 min. Cells were then treated with 50 mM NH_4Cl/PBS for 10 min at room temperature and blocked with PBS containing 3% BSA for 15 min. Primary antibodies were diluted 1:500 or 1:1,000, and Alexa Fluor–conjugated secondary antibodies (Invitrogen) were diluted 1:1,000 in PBS containing 3% BSA. Coverslips were incubated with primary antibodies for 60 min, washed six times with PBS, and incubated with secondary antibodies for 60 min. Samples were mounted using Slow Fade Gold and observed with an laser confocal microscope (FV1000; Olympus). The microscope images were taken using the FV1000 confocal laser-scanning microscope system equipped with a 100×/NA 1.40 oil immersion objective lens. Fluorochromes associated with the secondary antibodies were Alexa Fluor 405, 488, 568, or 594. Image acquisition software used was Fluoview (Olympus). The images were adjusted using Photoshop CS4 software (Adobe). For live-cell imaging, cells were grown in DMEM D6434 (Sigma-Aldrich) supplemented with 10% FBS with antibiotics on a glass-bottom dish (D310300; Matsunami Glass) and transfected with Effectene-coated latex beads for 30 min as previously described (Kobayashi et al., 2010). After beads transfection, the glass-bottom dish was mounted onto the microscope stage, which was equipped with a humidified environment chamber (MI-IBC; Olympus) that maintained the dish at 37°C with 5% CO_2. Images were acquired using an inverted microscope (model IX81; Olympus) equipped with a 60×/1.40 NA oil immersion objective (Olympus), a xenon lamp, a cooled charge-coupled device camera (CoolSNAP HQ; Roper Scientific), and a ZDC system under the control of MetaMorph v7.6.5.0 (Molecular Devices, MDS Analytical Technologies).

GST pull-down assay

GST and GST-Ub were purified from *Escherichia coli* lysates over glutathione Sepharose 4B (GE Healthcare) and dialyzed in PBS. 30 µg of each GST protein immobilized on 30 µl of glutathione Sepharose 4B was used per binding reaction. Mammalian cell lysates or bacterial cell lysates were used as the input proteins. HEK293T cells were transiently transfected with plasmids encoding the indicated Atg16L1 constructs, homogenized in PBS containing protease inhibitors (complete protease inhibitor cocktail; Roche), and then cleared by centrifugation and filtration (0.22 µm). Alternatively, *E. coli* BL-21 (DE3) cells expressing trigger factor–fused FLAG-WD β-propellers of Atg16L1 were sonicated in PBS containing 0.01% Triton X-100 and protease inhibitors and cleared by centrifugation and filtration (0.22 µm). Immobilized beads and cell lysates were incubated in a total volume of 500 µl PBS containing 0.1 mg/ml BSA and 0.01% Triton X-100 with gentle agitation for 1 h at 25°C. The beads were washed three times with ice-cold PBS and the bound complexes were eluted with 50 mM reduced glutathione in PBS and then subjected to SDS-PAGE and Western blot analyses.

Fractionation of bead–autophagosomes

Bead–autophagosomes were isolated using a modification of the method described by Desjardins et al. (1994). HeLa cells were transfected with Effectene-coated beads and incubated for 3 h. The cells were harvested with a silicone rubber scraper and homogenized in buffer (20 mM Hepes-KOH, pH 7.4, 80 mM sucrose, 220 mM mannitol, 10 mM *N*-ethylmaleimide, 1 mM PMSF, and a protease inhibitor cocktail [Roche]) by repeatedly passing (~15 times) through a 1-ml syringe with a 25-gauge needle. The homogenate was centrifuged at 1,000 *g* for 10 min to remove the cytosol and microsomes. The bead–autophagosomes were isolated by flotation on a discontinuous gradient composed of 1 ml each of increasing concentrations of sucrose solutions (60, 40, 35, 30, 25, 20, 15, 10, and 5%; all sucrose solutions were wt/wt in 3 mM imidazole, pH 7.4). The resulting pellet was resuspended in a 25% sucrose solution and loaded on top of a 30% sucrose solution. The samples were centrifuged in a swinging bucket rotor (SW41Ti; Beckman Coulter) for 1 h at 100,000 *g* at 4°C. The bead-autophagosome–containing fraction was collected from the interface of the 10 and 15% sucrose solution. The bead–autophagosomes were resuspended in 2 ml of ice-cold PBS and pelleted by centrifuging for 10 min at 20,000 *g* at 4°C.

Yeast two-hybrid assays

Yeast two-hybrid assays were performed using the Matchmaker GAL4 Yeast Two Hybrid 3 system (Takara Bio Inc.) as previously reported (Langelier et al., 2006). *Saccharomyces cerevisiae* AH-109 was cotransformed with the cloning vectors, pGADT7 or pGBKT7, containing the inserts of interest. The transformed yeast cells were incubated on yeast nitrogen base and glucose with minus Leu, minus Trp selection for 3 d at 30°C. 10–100 colonies were resuspended in a liquid culture of Sabourand dextrose broth (minus Leu, minus Trp), and incubated on Sabourand dextrose broth (minus Leu, minus Trp, minus Ade, minus His) plates for 3 d.

Identification of co-purifying proteins by mass spectrometry

HEK293T cells were seeded (3 × 10^6 cells/55-cm^2 dish) and cotransfected with 3 µg each of plasmids encoding members of the Atg16L1 complex (Atg12, Atg5, and Atg16L1) using polyethylenimine (25,000 kD; Polysciences, Inc.) as previously described (Durocher et al., 2002). The cells were harvested 48 h after transfection by incubating in 300 µl lysis buffer (50 mM Tris, pH 7.4, and 150 mM NaCl) supplemented with proteinase inhibitor cocktail (Roche) and 1% Triton X-100. Lysates were clarified by centrifugation (18,000 *g*, 10 min, 4°C) and incubated with Strep-Tactin Sepharose (30 µl slurry, 2 h, 4°C; IBA GmbH). The matrix was washed four times in wash buffer (20 mM Tris, pH 7.4, and 150 mM NaCl) supplemented with 0.1% Triton X-100, and the purified Atg16L1 complexes were eluted with 2.5 mM desthiobiotin. The co-purified proteins were identified by mass spectrometry. Briefly, the co-purified proteins were identified after SDS-PAGE and band excision. The proteins were digested with trypsin and identified by separating the peptide mixtures using nano-flow liquid chromatography with online tandem mass spectrometry (LC-MS/MS). Tandem mass spectra were acquired automatically and then searched against a nonredundant human database from the NCBI database with the Mascot Server (Matrix Science).

Statistics

All values in the figures are shown with standard deviation. Statistical analyses were performed using a two-tailed unpaired *t* test. P values <0.05 were considered statistically significant.

Online supplemental materials

Fig. S1 shows the result of hierarchal analysis of Atg proteins in bead-transfected cells. Fig. S2 shows localization of K48- and K63-linked Ub chains to the invading *Salmonella* or transfected beads, and loss of function effect of K63- or linear-linked Ub chains on selective autophagy. Fig. S3 shows the purity of the recombinant proteins for the GST pull-down assay. Fig. S4 shows the effect of deletion of WDR in Atg16L1 on the order of the Atg16L1 and ULK1-FIP200 complex recruitment to Ub-positive *Salmonella*. Fig. S5 shows the effect of Atg16L1 mutations on canonical and selective autophagy against transfected beads. Videos show dynamics of LC3 and galectin3 (Video 1), Ub and galectin3 (Video 2), LC3 and Ub (Video 3), Atg5 and Ub (Video 4), WIPI-1 and Ub (Video 5), Atg14L and Ub (Video 6), or ULK1 and Ub (Video 7) in autophagy against transfected beads. Table S1 provides a list of FIP200 peptides detected by affinity purification with the Atg16L1 complex and mass spectrometry analysis. Online supplemental material is available at http://www.jcb.org/cgi/content/full/jcb.201304188/DC1.

The authors thank R.Y. Tsien for the gift of mStrawberry cDNA; S. Yamaoka for providing pMRX-IRES-puro and pMRX-IRES-bsr; T. Kitamura for providing the Plat-E cells; N. Mizushima for the anti-Atg16L1 antibody; K. Okamoto for helpful discussions; S. Cox for English editing of the manuscript; and R. Tsukahara and H. Akai for technical assistance. LC-MS/MS analysis was performed in the DNA-chip Development Center for Infectious Diseases (RIMD, Osaka University).

This work was supported in part by the Ministry of Education, Culture, Sports, Science and Technology (MEXT; to N. Fujita, S. Kobayashi, T. Haraguchi, T. Noda, and T. Yoshimori); and the Takeda Science Foundation (to T. Yoshimori and T. Noda).

Submitted: 29 April 2013
Accepted: 4 September 2013

Published October 7, 2013

References

Birmingham, C.L., and J.H. Brumell. 2006. Autophagy recognizes intracellular *Salmonella enterica* serovar Typhimurium in damaged vacuoles. *Autophagy*. 2:156–158.

Desjardins, M., L.A. Huber, R.G. Parton, and G. Griffiths. 1994. Biogenesis of phagolysosomes proceeds through a sequential series of interactions with the endocytic apparatus. *J. Cell Biol.* 124:677–688. http://dx.doi.org/10.1083/jcb.124.5.677

Dupont, N., S. Lacas-Gervais, J. Bertout, I. Paz, B. Freche, G.T. Van Nhieu, F.G. van der Goot, P.J. Sansonetti, and F. Lafont. 2009. *Shigella* phagocytic vacuolar membrane remnants participate in the cellular response to pathogen invasion and are regulated by autophagy. *Cell Host Microbe*. 6:137–149. http://dx.doi.org/10.1016/j.chom.2009.07.005

Durocher, Y., S. Perret, and A. Kamen. 2002. High-level and high-throughput recombinant protein production by transient transfection of suspension-growing human 293-EBNA1 cells. *Nucleic Acids Res.* 30:E9. http://dx.doi.org/10.1093/nar/30.2.e9

Fujita, N., M. Hayashi-Nishino, H. Fukumoto, H. Omori, A. Yamamoto, T. Noda, and T. Yoshimori. 2008a. An Atg4B mutant hampers the lipidation of LC3 paralogues and causes defects in autophagosome closure. *Mol. Biol. Cell*. 19:4651–4659. http://dx.doi.org/10.1091/mbc.E08-03-0312

Fujita, N., T. Itoh, H. Omori, M. Fukuda, T. Noda, and T. Yoshimori. 2008b. The Atg16L complex specifies the site of LC3 lipidation for membrane biogenesis in autophagy. *Mol. Biol. Cell*. 19:2092–2100. http://dx.doi.org/10.1091/mbc.E07-12-1257

Fujita, N., T. Saitoh, S. Kageyama, S. Akira, T. Noda, and T. Yoshimori. 2009. Differential involvement of Atg16L1 in Crohn disease and canonical autophagy: analysis of the organization of the Atg16L1 complex in fibroblasts. *J. Biol. Chem.* 284:32602–32609. http://dx.doi.org/10.1074/jbc.M109.037671

Fujita, N., and T. Yoshimori. 2011. Ubiquitination-mediated autophagy against invading bacteria. *Curr. Opin. Cell Biol.* 23:492–497. http://dx.doi.org/10.1016/j.ceb.2011.03.003

Hara, T., and N. Mizushima. 2009. Role of ULK-FIP200 complex in mammalian autophagy: FIP200, a counterpart of yeast Atg17? *Autophagy*. 5:85–87. http://dx.doi.org/10.4161/auto.5.1.7180

Hofmann, R.M., and C.M. Pickart. 1999. Noncanonical MMS2-encoded ubiquitin-conjugating enzyme functions in assembly of novel polyubiquitin chains for DNA repair. *Cell*. 96:645–653. http://dx.doi.org/10.1016/S0092-8674(00)80575-9

Huett, A., R.J. Heath, J. Begun, S.O. Sassi, L.A. Baxt, J.M. Vyas, M.B. Goldberg, and R.J. Xavier. 2012. The LRR and RING domain protein LRSAM1 is an E3 ligase crucial for ubiquitin-dependent autophagy of intracellular *Salmonella* Typhimurium. *Cell Host Microbe*. 12:778–790. http://dx.doi.org/10.1016/j.chom.2012.10.019

Itakura, E., and N. Mizushima. 2010. Characterization of autophagosome formation site by a hierarchical analysis of mammalian Atg proteins. *Autophagy*. 6:764–776. http://dx.doi.org/10.4161/auto.6.6.12709

Itakura, E., C. Kishi-Itakura, I. Koyama-Honda, and N. Mizushima. 2012. Structures containing Atg9A and the ULK1 complex independently target depolarized mitochondria at initial stages of Parkin-mediated mitophagy. *J. Cell Sci.* 125:1488–1499. http://dx.doi.org/10.1242/jcs.094110

Itoh, T., N. Fujita, E. Kanno, A. Yamamoto, T. Yoshimori, and M. Fukuda. 2008. Golgi-resident small GTPase Rab33B interacts with Atg16L and modulates autophagosome formation. *Mol. Biol. Cell*. 19:2916–2925. http://dx.doi.org/10.1091/mbc.E07-12-1231

Iwai, K., and F. Tokunaga. 2009. Linear polyubiquitination: a new regulator of NF-kappaB activation. *EMBO Rep.* 10:706–713. http://dx.doi.org/10.1038/embor.2009.144

Kageyama, S., H. Omori, T. Saitoh, T. Sone, J.L. Guan, S. Akira, F. Imamoto, T. Noda, and T. Yoshimori. 2011. The LC3 recruitment mechanism is separate from Atg9L1-dependent membrane formation in the autophagic response against *Salmonella*. *Mol. Biol. Cell*. 22:2290–2300. http://dx.doi.org/10.1091/mbc.E10-11-0893

Katzmann, D.J., M. Babst, and S.D. Emr. 2001. Ubiquitin-dependent sorting into the multivesicular body pathway requires the function of a conserved endosomal protein sorting complex, ESCRT-I. *Cell*. 106:145–155. http://dx.doi.org/10.1016/S0092-8674(01)00434-2

Kimura, S., N. Fujita, T. Noda, and T. Yoshimori. 2009. Monitoring autophagy in mammalian cultured cells through the dynamics of LC3. *Methods Enzymol.* 452:1–12. http://dx.doi.org/10.1016/S0076-6879(08)03601-X

Kobayashi, S., T. Kojidani, H. Osakada, A. Yamamoto, T. Yoshimori, Y. Hiraoka, and T. Haraguchi. 2010. Artificial induction of autophagy around polystyrene beads in nonphagocytic cells. *Autophagy*. 6:36–45. http://dx.doi.org/10.4161/auto.6.1.10324

Kuma, A., M. Hatano, M. Matsui, A. Yamamoto, H. Nakaya, T. Yoshimori, Y. Ohsumi, T. Tokuhisa, and N. Mizushima. 2004. The role of autophagy during the early neonatal starvation period. *Nature*. 432:1032–1036. http://dx.doi.org/10.1038/nature03029

Langelier, C., U.K. von Schwedler, R.D. Fisher, I. De Domenico, P.L. White, C.P. Hill, J. Kaplan, D. Ward, and W.I. Sundquist. 2006. Human ESCRT-II complex and its role in human immunodeficiency virus type 1 release. *J. Virol.* 80:9465–9480. http://dx.doi.org/10.1128/JVI.01049-06

Matsunaga, K., T. Saitoh, K. Tabata, H. Omori, T. Satoh, N. Kurotori, I. Maejima, K. Shirahama-Noda, T. Ichimura, T. Isobe, et al. 2009. Two Beclin 1-binding proteins, Atg14L and Rubicon, reciprocally regulate autophagy at different stages. *Nat. Cell Biol.* 11:385–396. http://dx.doi.org/10.1038/ncb1846

Mizushima, N. 2010. The role of the Atg1/ULK1 complex in autophagy regulation. *Curr. Opin. Cell Biol.* 22:132–139. http://dx.doi.org/10.1016/j.ceb.2009.12.004

Mizushima, N., A. Kuma, Y. Kobayashi, A. Yamamoto, M. Matsubae, T. Takao, T. Natsume, Y. Ohsumi, and T. Yoshimori. 2003. Mouse Apg16L, a novel WD-repeat protein, targets to the autophagic isolation membrane with the Apg12-Apg5 conjugate. *J. Cell Sci.* 116:1679–1688. http://dx.doi.org/10.1242/jcs.00381

Mizushima, N., B. Levine, A.M. Cuervo, and D.J. Klionsky. 2008. Autophagy fights disease through cellular self-digestion. *Nature*. 451:1069–1075. http://dx.doi.org/10.1038/nature06639

Morita, S., T. Kojima, and T. Kitamura. 2000. Plat-E: an efficient and stable system for transient packaging of retroviruses. *Gene Ther.* 7:1063–1066. http://dx.doi.org/10.1038/sj.gt.3301206

Newton, K., M.L. Matsumoto, I.E. Wertz, D.S. Kirkpatrick, J.R. Lill, J. Tan, D. Dugger, N. Gordon, S.S. Sidhu, F.A. Fellouse, et al. 2008. Ubiquitin chain editing revealed by polyubiquitin linkage-specific antibodies. *Cell*. 134:668–678. http://dx.doi.org/10.1016/j.cell.2008.07.039

Nishimura, T., T. Kaizuka, K. Cadwell, M.H. Sahani, T. Saitoh, S. Akira, H.W. Virgin, and N. Mizushima. 2013. FIP200 regulates targeting of Atg16L1 to the isolation membrane. *EMBO Rep.* 14:284–291. http://dx.doi.org/10.1038/embor.2013.6

Pashkova, N., L. Gakhar, S.C. Winistorfer, L. Yu, S. Ramaswamy, and R.C. Piper. 2010. WD40 repeat propellers define a ubiquitin-binding domain that regulates turnover of F box proteins. *Mol. Cell*. 40:433–443. http://dx.doi.org/10.1016/j.molcel.2010.10.018

Paz, I., M. Sachse, N. Dupont, J. Mounier, C. Cederfur, J. Enninga, H. Leffler, F. Poirier, M.C. Prevost, F. Lafont, and P. Sansonetti. 2010. Galectin-3, a marker for vacuole lysis by invasive pathogens. *Cell. Microbiol.* 12:530–544. http://dx.doi.org/10.1111/j.1462-5822.2009.01415.x

Saitoh, T., M. Nakayama, H. Nakano, H. Yagita, N. Yamamoto, and S. Yamaoka. 2003. TWEAK induces NF-kappaB2 p100 processing and long lasting NF-kappaB activation. *J. Biol. Chem.* 278:36005–36012. http://dx.doi.org/10.1074/jbc.M304266200

Saitoh, T., N. Fujita, M.H. Jang, S. Uematsu, B.G. Yang, T. Satoh, H. Omori, T. Noda, N. Yamamoto, M. Komatsu, et al. 2008. Loss of the autophagy protein Atg16L1 enhances endotoxin-induced IL-1beta production. *Nature*. 456:264–268. http://dx.doi.org/10.1038/nature07383

Saitoh, T., N. Fujita, T. Hayashi, K. Takahara, T. Satoh, H. Lee, K. Matsunaga, S. Kageyama, H. Omori, T. Noda, et al. 2009. Atg9a controls dsDNA-driven dynamic translocation of STING and the innate immune response. *Proc. Natl. Acad. Sci. USA*. 106:20842–20846. http://dx.doi.org/10.1073/pnas.0911267106

Shahnazari, S., W.L. Yen, C.L. Birmingham, J. Shiu, A. Namolovan, Y.T. Zheng, K. Nakayama, D.J. Klionsky, and J.H. Brumell. 2010. A diacylglycerol-dependent signaling pathway contributes to regulation of antibacterial autophagy. *Cell Host Microbe*. 8:137–146. http://dx.doi.org/10.1016/j.chom.2010.07.002

Suzuki, K., and Y. Ohsumi. 2010. Current knowledge of the pre-autophagosomal structure (PAS). *FEBS Lett.* 584:1280–1286. http://dx.doi.org/10.1016/j.febslet.2010.02.001

Thurston, T.L., G. Ryzhakov, S. Bloor, N. von Muhlinen, and F. Randow. 2009. The TBK1 adaptor and autophagy receptor NDP52 restricts the proliferation of ubiquitin-coated bacteria. *Nat. Immunol.* 10:1215–1221. http://dx.doi.org/10.1038/ni.1800

Thurston, T.L., M.P. Wandel, N. von Muhlinen, A. Foeglein, and F. Randow. 2012. Galectin 8 targets damaged vesicles for autophagy to defend cells against bacterial invasion. *Nature*. 482:414–418. http://dx.doi.org/10.1038/nature10744

Tokunaga, F., S. Sakata, Y. Saeki, Y. Satomi, T. Kirisako, K. Kamei, T. Nakagawa, M. Kato, S. Murata, S. Yamaoka, et al. 2009. Involvement of linear polyubiquitylation of NEMO in NF-kappaB activation. *Nat. Cell Biol.* 11:123–132. http://dx.doi.org/10.1038/ncb1821

van Wijk, S.J., E. Fiskin, M. Putyrski, F. Pampaloni, J. Hou, P. Wild, T. Kensche, H.E. Grecco, P. Bastiaens, and I. Dikic. 2012. Fluorescence-based sensors to monitor localization and functions of linear and K63-linked ubiquitin chains in cells. *Mol. Cell*. 47:797–809. http://dx.doi.org/10.1016/j.molcel.2012.06.017

Published October 7, 2013

Wild, P., H. Farhan, D.G. McEwan, S. Wagner, V.V. Rogov, N.R. Brady, B. Richter, J. Korac, O. Waidmann, C. Choudhary, et al. 2011. Phosphorylation of the autophagy receptor optineurin restricts *Salmonella* growth. *Science*. 333:228–233. http://dx.doi.org/10.1126/science.1205405

Yamamoto, M., T. Okamoto, K. Takeda, S. Sato, H. Sanjo, S. Uematsu, T. Saitoh, N. Yamamoto, H. Sakurai, K.J. Ishii, et al. 2006. Key function for the Ubc13 E2 ubiquitin-conjugating enzyme in immune receptor signaling. *Nat. Immunol.* 7:962–970. http://dx.doi.org/10.1038/ni1367

Yang, Y., J. Kitagaki, R.M. Dai, Y.C. Tsai, K.L. Lorick, R.L. Ludwig, S.A. Pierre, J.P. Jensen, I.V. Davydov, P. Oberoi, et al. 2007. Inhibitors of ubiquitin-activating enzyme (E1), a new class of potential cancer therapeutics. *Cancer Res.* 67:9472–9481. http://dx.doi.org/10.1158/0008-5472.CAN-07-0568

Yoshikawa, Y., M. Ogawa, T. Hain, M. Yoshida, M. Fukumatsu, M. Kim, H. Mimuro, I. Nakagawa, T. Yanagawa, T. Ishii, et al. 2009. Listeria monocytogenes ActA-mediated escape from autophagic recognition. *Nat. Cell Biol.* 11:1233–1240. http://dx.doi.org/10.1038/ncb1967

Youle, R.J., and D.P. Narendra. 2011. Mechanisms of mitophagy. *Nat. Rev. Mol. Cell Biol.* 12:9–14. http://dx.doi.org/10.1038/nrm3028

Zheng, Y.T., S. Shahnazari, A. Brech, T. Lamark, T. Johansen, and J.H. Brumell. 2009. The adaptor protein p62/SQSTM1 targets invading bacteria to the autophagy pathway. *J. Immunol.* 183:5909–5916. http://dx.doi.org/10.4049/jimmunol.0900441

Please cite this article in press as: Suzuki et al., Structural Basis of the Autophagy-Related LC3/Atg13 LIR Complex: Recognition and Interaction Mechanism, Structure (2014), http://dx.doi.org/10.1016/j.str.2013.09.023

Structure
Article

Structural Basis of the Autophagy-Related LC3/Atg13 LIR Complex: Recognition and Interaction Mechanism

Hironori Suzuki,[1,2,*] Keisuke Tabata,[3,4] Eiji Morita,[3] Masato Kawasaki,[2] Ryuichi Kato,[2] Renwick C.J. Dobson,[1,5,*] Tamotsu Yoshimori,[4,6] and Soichi Wakatsuki[2,7,8]
[1]Biomolecular Interaction Centre, School of Biological Sciences, University of Canterbury, Christchurch 8020, New Zealand
[2]Structural Biology Research Center, Photon Factory, Institute of Materials Structure Science, High Energy Accelerator Research Organization (KEK), Tsukuba, Ibaraki 305-0801, Japan
[3]International Research Center for Infectious Diseases, Research Institute for Microbial Diseases, Osaka University, Osaka 565-0871, Japan
[4]Department of Genetics, Graduate School of Medicine, Osaka University, Suita, Osaka 565-0871, Japan
[5]Department of Biochemistry and Molecular Biology, Bio21 Institute, University of Melbourne, Parkville, Victoria 3010, Australia
[6]Laboratory of Intracellular Membrane Dynamics, Graduate School of Frontier Biosciences, Osaka University, Suita, Osaka 565-0871, Japan
[7]Photon Science, SLAC National Accelerator Laboratory, Menlo Park, CA 94025-7015, USA
[8]Department of Structural Biology, School of Medicine, Stanford University, Stanford, CA 94305-5126, USA
*Correspondence: hironori.suzuki@canterbury.ac.nz (H.S.), renwick.dobson@canterbury.ac.nz (R.C.J.D.)
http://dx.doi.org/10.1016/j.str.2013.09.023

SUMMARY

Autophagy is a bulk degradation pathway that removes cytosolic materials to maintain cellular homeostasis. The autophagy-related gene 13 (Atg13) and microtubule associate protein 1 light chain 3 (LC3) proteins are required for autophagosome formation. We demonstrate that each of the human LC3 isoforms (LC3A, LC3B, and LC3C) interacts with Atg13 via the LC3 interacting region (LIR) of Atg13. Using X-ray crystallography, we solved the macromolecular structures of LC3A and LC3C, along with the complex structures of the LC3 isoforms with the Atg13 LIR. Together, our structural and binding analyses reveal that the side-chain of Lys49 of LC3 acts as a gatekeeper to regulate binding of the LIR. We verified this observation by mutation of Lys49 in LC3A, which significantly reduces LC3A positive puncta formation in cultured cells. Our results suggest that specific affinity of the LC3 isoforms to the Atg13 LIR is required for proper autophagosome formation.

INTRODUCTION

Autophagy is an essential intracellular process that maintains cellular homeostasis by degrading proteins, organelles, and bacterial pathogens. Dysfunction of the autophagy pathway causes a range of diseases in humans, including cancers, the neurodegenerative diseases such as Alzheimer's and Parkinson's, myopathies, and heart and liver diseases (Mizushima et al., 2008; Levine and Kroemer, 2008; Dikic et al., 2010). The process is widely conserved, from yeast to higher eukaryotes.

Autophagy has been particularity well characterized in yeast. Here, the process is initiated by the autophagy-related gene 1 complex (the Atg1 complex), which consists of Atg1 (Kamada et al., 2000), Atg13 (Funakoshi et al., 1997), Atg17 (Kamada et al., 2000), Atg29 (Kawamata et al., 2005) and Atg31 (Kabeya et al., 2007). Atg1 complex formation is regulated by target of rapamycin complex 1 (TORC1) and protein kinase A (PKA). Under stress-free conditions, the Atg1 complex is phosphorylated and inactivated by TORC1 and PKA. However, upon the induction of autophagy by intracellular signals (nutrient starvation or endoplasmic reticulum stress) or extracellular signals (invasion of pathogens), TORC1 and PKA are switched off, activating autophagy by allowing the Atg1 serine/threonine kinase to phosphorylate the Atg1 complex. The Atg1 complex is then recruited to double membrane structures, known as isolation membranes.

In human cells, Atg1 and Atg13 are conserved, although Atg1 is known as Unc-51-like kinase 1 (ULK1; Chan et al., 2007, 2009). The human homologs of Atg17, Atg29, and Atg31 are not reported; however, the focal adhesion kinase family interacting protein of 200 kDa (FIP200) is thought to play the role of Atg17 (Hara et al., 2008), and Atg101 has been identified as a component of the human Atg1 complex, called the ULK1 complex (Hosokawa et al., 2009). It was recently reported that Atg8 interacts with the Atg1 protein via the W/Y/FxxL/I/V motif (known as the LC3-interaction region [LIR]) promoting Atg1 degradation in the vacuole by recruiting the complex to the autophagosome (Kraft et al., 2012).

Atg8 is one of the autophagy-related genes that are indispensable for autophagosome formation, membrane tethering, and hemifusion (Nakatogawa et al., 2007). In yeast, only one Atg8 protein has been identified, whereas in human cells, seven Atg8 homolog proteins are reported and these are categorized into three subfamilies: microtubule associate protein 1 light chain 3 (which we call LC3A, LC3B, and LC3C in this work), γ-amino-butyric acid receptor-associated protein (GABARAP, GABARAPL-1, and GABARAPL-3), and golgi-associated adenosine triphosphatase enhancer of 16 kDa (GATE-16, also known as GABARAPL-2; He et al., 2003; Xin et al., 2001).

These Atg8 family proteins undergo multistep modifications: first by the cysteine protease Atg4, then the E1-like (ubiquitin

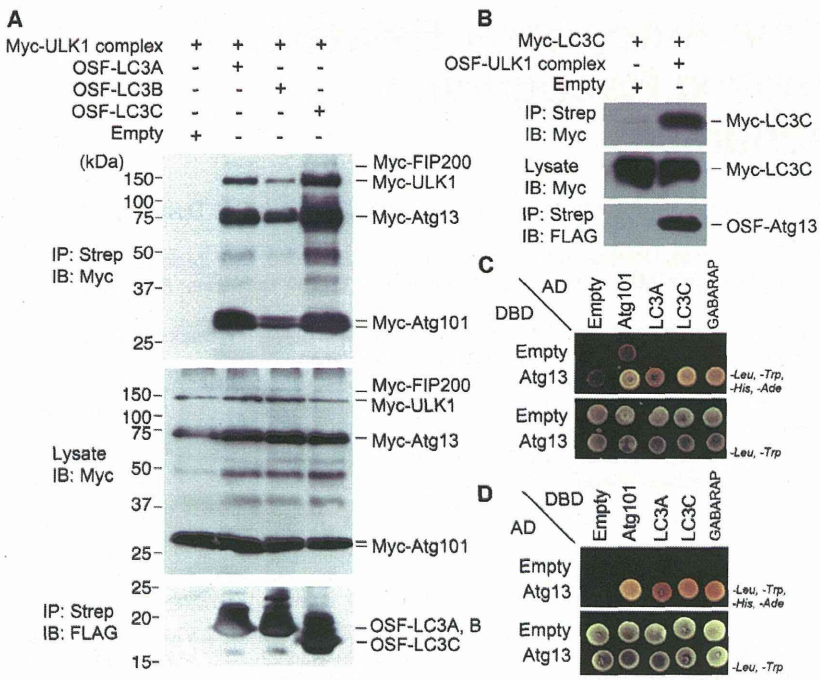

Figure 1. The ULK1 Complex Interacts with LC3 Family Proteins

(A) Myc-ULK1 complex (mixture of Myc-Atg13, Myc-Atg101, Myc-ULK1, and Myc-FIP200) coprecipitate with empty vector controls (lane 1), OSF-LC3A (lane 2), OSF-LC3B (lane 3), or OSF-LC3C (lane 4).

(B) ULK1 complexes coprecipitate with LC3C. Myc-LC3C coprecipitations with empty vector controls (lane 1), OSF-Atg13 (lane 2).

(C and D) Directed yeast two-hybrid interactions between human Atg13 and LC3 family proteins. The top array shows doubly transformed yeast replica plated on minus Leu, minus Trp, minus His, minus Ade selection media, where successful growth represents a positive protein interaction. The bottom array shows replica-plated yeast on minus Leu, minus Trp media (a control for equivalent transformation and yeast growth). The indicated constructs were fused to activating domains (ADs) or DNA binding domains (DBDs). Unfused DBD and AD constructs are shown as negative controls.

activating) enzyme Atg7, and finally the E2-like (ubiquitin conjugating) enzyme Atg3; as a result, they are conjugated to the autophagosome membrane in the following manner. In the first step, newly synthesized Atg8 family proteins are immediately cleaved at its C terminus by Atg4, resulting in the exposure of the C-terminal conserved glycine residue (Hemelaar et al., 2003; He et al., 2003; Tanida et al., 2004; Li et al., 2011). Atg7 forms a thioester intermediate with Atg8, followed by the conjugation of phosphatidylethanolamine by Atg3, which anchors the Atg8 family proteins to the autophagosome membrane (Schlumpberger et al., 1997; Tanida et al., 1999; Taherbhoy et al., 2011). In this process, Atg8 family proteins play a role not only in the elongation of the autophagosome membrane, but also in the recruitment of specific cytosolic materials to the autophagosome membrane, such as unfolded or aggregated proteins, mitochondria, and bacterial pathogens, via adaptor proteins that have the LIR motif. Hence, the process is called selective autophagy (Ichimura and Komatsu, 2010; Johansen and Lamark, 2011).

Five Atg8 structures in complex with LIRs have been reported: Atg8/Atg19 (Noda et al., 2008); LC3/Atg4B (Satoo et al., 2009); LC3B/p62 (Noda et al., 2008; Ichimura et al., 2008); LC3C/NDP52 (von Muhlinen et al., 2012); and GABARAP/neighbor of BRCA1 gene 1 (NBR1; Rozenknop et al., 2011). Despite these studies, the interaction mechanism remains unknown, although it has been demonstrated that the side-chains of Trp/Phe/Tyr and Leu/Ile/Val recognize two different hydrophobic surfaces on Atg8 proteins, named the W- and L-sites by Noda et al. (2010). Recently, Alemu et al. (2012) reported that Atg8 family proteins directly interact with ULK1, Atg13, and FIP200, members of the Atg1/ULK1 complex, through the LIR, and characterized ULK1 and Atg13 LIR motifs binding to GABARAP. The ULK1 LIR motif is required for starvation-induced autophagosome formation (Alemu et al., 2012).

In this article, we describe the binding interaction between Atg13 and LC3. Employing in vitro binding assays, we have independently determined that Atg13 directly interacts with LC3 via the LIR located at its C terminus. To probe the structural basis and mechanism of this interaction, we have used X-ray crystallography to solve the structures of LC3A and LC3C, along with the structures of LC3 isoforms in complex with a peptide containing the residues 436–447 of Atg13, which includes the LC3 interaction region W/Y/FxxL/I/V. Structural comparison reveals that binding of the LIR to LC3 induces a structural change of the side-chain of Lys49 of LC3, exposing a hydrophobic surface to accept the LIR. This movement is conserved in the LC3 family proteins. We verified the role of Lys49 by mutagenesis, which significantly reduces autophagosome formation. Together, our data demonstrate that Lys49 plays an important role in regulating the interaction with LIR-containing proteins in autophagy.

RESULTS

Atg13 Binds to LC3 Isoforms

The four known ULK1 complex subunits (ULK1, FIP200, Atg101, and Atg13), which included a One-STrEP-FLAG (OSF) tag, were simultaneously coexpressed in human embryonic kidney 293T cells (HEK293T) cells to create "baits" that could be used to identify ULK1 complex binding proteins. The resulting mixture of ULK1 complex proteins was affinity purified on a Strep-Tactin resin, which captured Atg13 and its binding partners. Bound proteins were separated by SDS-PAGE and identified by mass spectrometry analysis, which, remarkably, identified two different Atg8/LC3 family proteins as the ULK1 complex coprecipitates (LC3A and LC3C; data not shown). These interactions were initially verified by demonstrating that Myc-tagged ULK1 complexes bound to immobilized OSF-LC3A, OSF-LC3B, and OSF-LC3C, but not to control resins (Figure 1A). Reciprocal

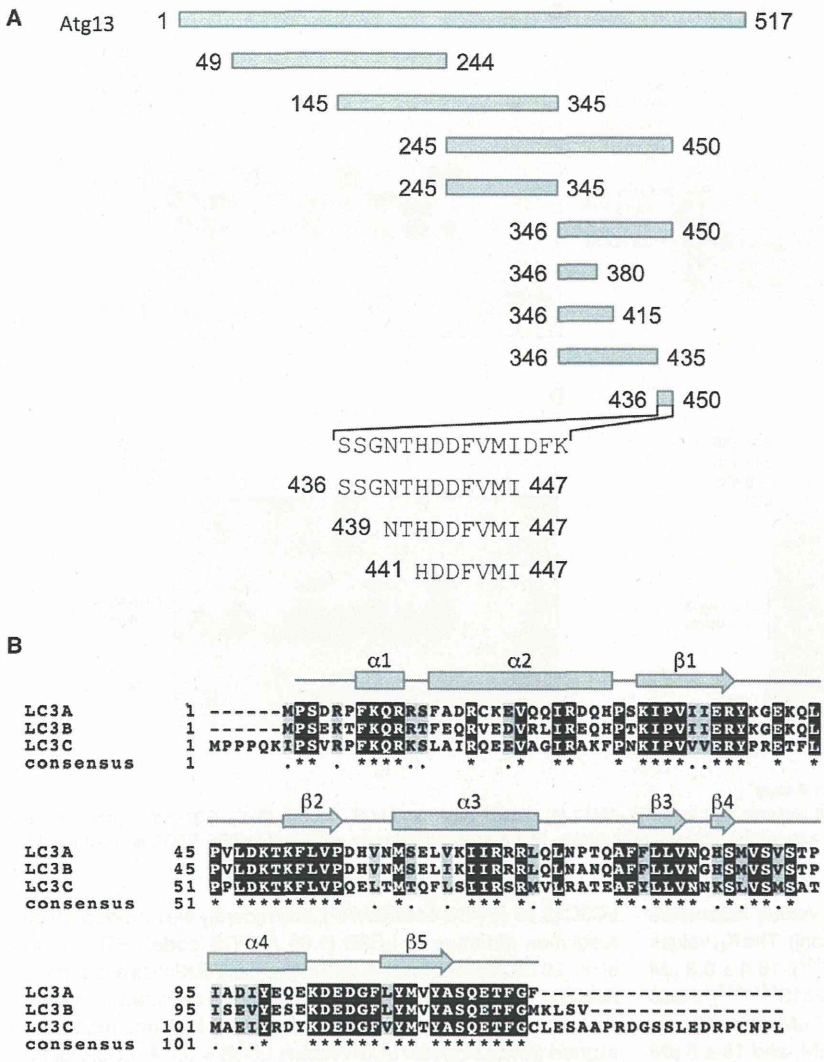

Figure 2. Schematic Representation of Atg13 and LC3 Isoforms

(A) The Atg13 deletion mutants and LIR peptides for the interaction analysis.

(B) Sequence alignment and secondary structure representation of LC3 isoforms. The multiple sequence alignment was generated by ClustalX2 (Larkin et al., 2007) using a box shade representation by BOXSHADE 3.21 (http://embnet.vital-it.ch/software/BOX_form.html). The bar shows the region of LC3A constructs that is used in this study (2–121) along with the secondary structures estimated using the DSSP program (Kabsch and Sander, 1983; boxes are α helices and arrows β strands).

interactions were also confirmed by testing that Myc-tagged LC3C bound specifically immobilized OSF-ULK1 complexes (Figure 1B). The LC3 family proteins also exhibited positive two-hybrid interactions with the Atg13 subunit, but not with the FIP200, ULK1, or Atg101 subunits (Figures 1C and 1D; data not shown). These results indicate that the Atg13 subunit of this complex is responsible for the interaction with the LC3 family proteins.

Mapping the LC3 Binding Region in Atg13

To determine the LC3 binding sites in Atg13, we performed glutathione S-transferase (GST) pulldown assays using a range of Atg13 truncated mutants and the three LC3 isoforms, LC3A, LC3B, and LC3C (Figure 2). Expressed proteins corresponding to the regions of 49–244, 145–345, and 245–450 of Atg13 were inserted into the pCold Trigger Factor (TF) vector and expressed in *E. coli* as 6xHis-TF fused proteins. The GST-LC3 proteins were bound to glutathione Sepharose 4B (GS4B) resin and mixed with 6xHis-TF-Atg13 constructs (Figure 3A). The 6xHis-Atg13$^{245–450}$ was pulled down with GST-LC3A and GST-LC3C, but not with GST-LC3B. For further investigation, we divided the region from 245 to 450 of Atg13 as shown in Figure 2A. These proteins were expressed in *E. coli* and immobilized on GS4B resin. GST-LC3s were cleaved by thrombin and separated using size exclusion chromatography. Purified LC3s were incubated with the resin immobilized with the GST-Atg13 constructs (Figures 3B–3D). All three LC3 isoforms bound to Atg13$^{346–450}$ and Atg13$^{436–450}$. Although initial binding experiments did not show binding between 6xHis-TF-Atg13 and GST-LC3B, further pulldown experiments using additional truncated LIR constructs demonstrated that 15 amino acids (436-SSGNTHDDFVMIDFK-450) is sufficient to be recognized by the three LC3 isoforms, whereas the mutants of Atg13 lacking residues 436–450 (346–380, 346–380, and 346–435) did not bind to LC3s. The LC3 binding region of Atg13 identified here includes a motif similar to the LIR reported previously, xxxW/YxxL/I/V, where x is an acidic residue (Noda et al., 2008; Ichimura et al., 2008; Noda et al., 2010; Atg13, 441-HDDFVMI-447) and corresponds to the region reported by Alemu et al. (2012). This investigation demonstrated that LC3 isoforms bind to Atg13 via the LIR motif.

Dissociation Constants for the LC3 Interaction with LIR

To characterize the interaction kinetics between the Atg13 LIR variants and LC3s, we performed real-time interaction analysis using a surface plasmon resonance (SPR) biosensor, three GST-tagged constructs of the Atg13 LIR (436–447, 439–447 and 441–447), and the LC3A, LC3B, and LC3C isoforms. A range of concentrations of each LC3 isoform were injected onto the GST-Atg13 LIR peptides immobilized to a sensor chip via an anti-GST antibody. All three LC3 proteins demonstrated concentration-dependent increases in resonance signals (Figure S1 available online). The apparent dissociation constants (K_D) for the Atg13 LIR peptide/LC3s interaction were calculated using

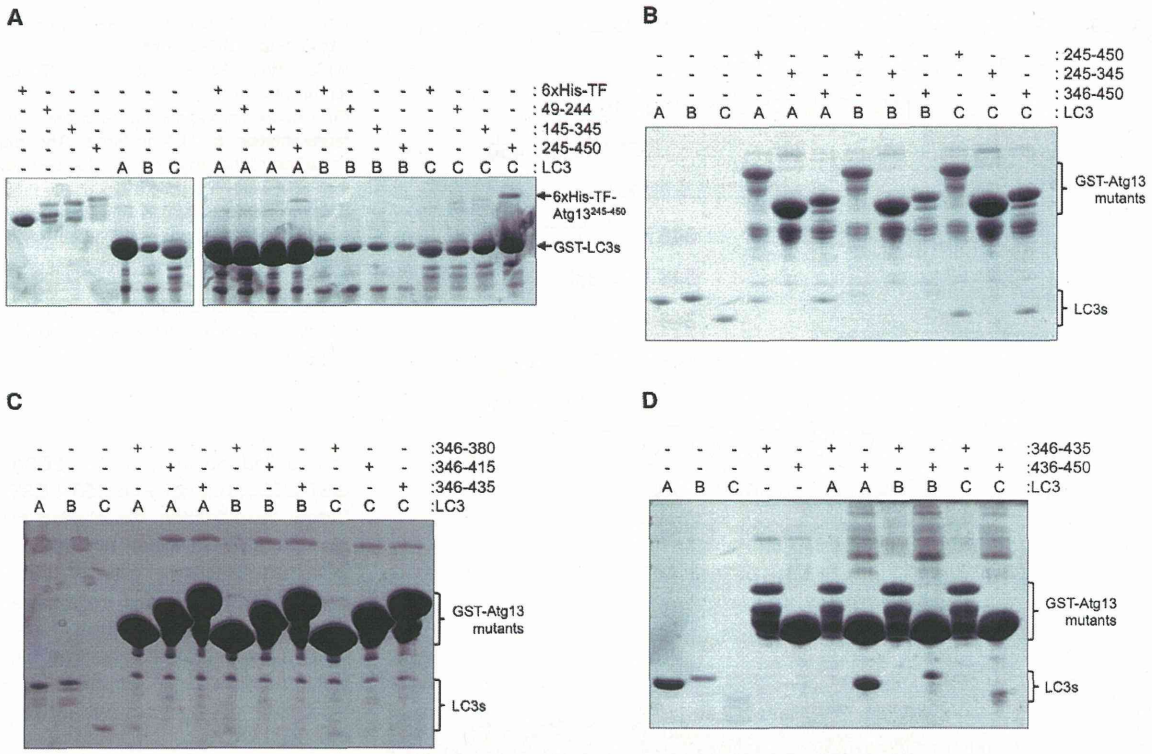

Figure 3. Identification of Atg13 LIR by Pulldown Assay

GST pulldown assays were performed using GST-LC3 isoforms and 6xHis-TF-Atg13 (A) or GST-Atg13 and LC3 isoforms (B–D). GST-fusion proteins were immobilized on Glutathione sepharose 4B and mixed with purified counterpart proteins. Pulldown products were subjected to SDS-PAGE and detected by Coomassie brilliant blue (CBB) staining.

the Scatchard plot analysis (resonance unit versus resonance unit/concentration [RU versus RU/concentration]). The K_D values for LC3A were 17.5 ± 0.2 μM (GST-Atg13$^{436–447}$), 16.4 ± 0.3 μM (GST-Atg13$^{439–447}$), and 18.3 ± 0.6 μM (GST-Atg13$^{441–447}$); those for LC3B were 57 ± 4 μM, 50 ± 3 μM, and 52 ± 7 μM, respectively; and those for LC3C were 12 ± 4 μM, 10 ± 3 μM, and 13 ± 6 μM (n = 3), respectively. Clearly, the addition of the N-terminal residues to the Atg13 LIR did not affect the binding affinities. The overall amino acid sequence identity between LC3A and LC3B is 83%, whereas between LC3A and LC3C, or LC3B and LC3C, it is only 55%. However, the binding affinity of LC3B to the Atg13 LIR is appreciably lower than that of LC3A or LC3C to Atg13 LIR. These data demonstrate that the region of Atg13 from 441 to 447 is sufficient to interact with LC3s and that LC3B may have a different LIR binding mode, given the lower affinity compared with LC3A and LC3C.

Structures of Uncomplexed Three LC3 Isoforms and the Isoforms in Complex with the Atg13 LIR

To elucidate the structural basis of the interaction between Atg13 and LC3s, we used X-ray crystallographic analysis to solve the structures of LC3A (2.00 Å; Protein Data Bank [PDB] code 3WAL) and LC3C (1.75 Å; PDB code 3WAM). In addition, we solved the complex forms of all three isoforms using chimeric proteins of Atg13$^{436–447}$-LC3A (1.77 Å; PDB code 3WAN), Atg13$^{436–447}$-LC3B (2.60 Å; PDB code 3WAO), and Atg13$^{436–447}$-LC3C (3.10 Å; PDB code 3WAP), and recently we reported a high-resolution structure of LC3B (1.60 Å; PDB code 3VTU; Rogov et al., 2013). Data collection and refinement statistics are summarized in Table 1 and the overall structures are depicted in Figure 4. Overall structures of the uncomplexed LC3 isoforms are closely aligned (RMSD values: LC3A versus LC3B = 0.7 Å, LC3A versus LC3C = 1.2 Å, LC3B versus LC3C = 1.3 Å), with noticeable differences in the loops between α3 and β4 and the region including β4, β5, and α4 (Figure 4). The asymmetric unit of the Atg13-LC3A contains two molecules, whereas the crystal structure of Atg13-LC3C contains only one and that of Atg13-LC3B contains four molecules, in which molecules A and B bind to molecules D and C, respectively (Figure S2). Interestingly, each of the chimeric molecules are packed within the crystal such that the Atg13$^{436–447}$ N-terminal region interacts, not with its fused LC3 domain, but with an LC3 domain related by the crystallographic symmetry (Atg13-LC3A, Atg13-LC3B, and Atg13-LC3C) and a noncrystallographic symmetry (Atg13-LC3B).

A comparison of the uncomplexed LC3 isoform structures to the Atg13-LC3 chimeric structures shows that the overall topologies are very similar. The electron density for the N terminus of the Atg13 LIR was not visible for Atg13-LC3A and Atg13-LC3B (residues Ser436 to His441) or for Atg13-LC3C (residues Ser436 to Glu443; Figure S3). This implies that the N terminus of the Atg13 LIR is not involved in the interaction, which is consistent with our detailed interaction experiments presented above

Table 1. Data Collection and Refinement Statistics

	LC3A	LC3C	$Atg13^{436–447}$-LC3A	$Atg13^{436–447}$-LC3B	$Atg13^{436–447}$-LC3C
PDB code	3WAL	3WAM	3WAN	3WAO	3WAP
Region of LC3	2–121	8–125	2–121	2–119	8–125
Data Collection					
Beamline	PF BL-17A	PF BL-5A	PF BL-17A	PF BL-17A	PF BL-17A
Wavelength (Å)	0.9800	1.0000	0.9800	0.9800	0.9800
Space group	$I4_1$	$P3_121$	$P2_1$	$P4_1$	$P3_121$
a, b, c (Å)	93.0, 93.0, 33.1	71.7, 71.7, 55.7	37.7, 47.9, 77.1	64.6, 64.6, 130.3	61.7, 61.7, 95.9
α, β, γ (°)	90.0, 90.0, 90.0	90.0, 90.0, 120.0	90.0, 94.2, 90.0	90.0, 90.0, 90.0	90.0, 90.0, 120.0
Resolution (Å)	46.5–2.00 (2.11–2.00)	27.8–1.75 (1.84–1.75)	47.9–1.77 (1.87–1.77)	43.4–2.60 (2.74–2.60)	53.5–3.10 (3.27–3.10)
Number of measured reflections	68,775 (10,192)	178,722 (25,835)	86,532 (11,807)	62,527 (8,938)	39,951 (6,084)
Number of unique reflections	9,793 (1,422)	16,985 (2,430)	24,414 (3,447)	16,435 (2,372)	4,045 (588)
Completeness (%)	100.0 (100.0)	99.8 (100.0)	99.0 (96.7)	99.9 (99.5)	98.5 (100.0)
R_{merge} (%)	7.4 (38.2)	9.3 (36.6)	5.9 (19.4)	6.8 (74.0)	6.9 (78.5)
I/σI	18.2 (5.1)	16.2 (6.3)	12.6 (4.9)	14.4 (2.4)	15.7 (2.8)
Refinement					
R_{work}/R_{free} (%)	18.1/23.7	17.2/23.7	17.4/22.7	22.3/29.4	21.0/26.6
Mean B value (Å^2)	35.1	23.7	18.7	61.5	144.7
Rmsd bond length (Å)	0.019	0.034	0.022	0.011	0.014
Rmsd bond angle (°)	1.943	2.446	2.145	1.801	2.445
Ramachandran plot					
Favored/allowed/outlier (%)	100/0/0	98.2/1.8/0	98.8/1.2/0	98.2/1.8/0	99.2/0.8/0
Number of molecules in the asymmetric unit	1	1	2	4	1

Highest resolution shell is shown in parentheses. rmsd, root-mean-square deviation.

in which truncated peptides 436–447, 439–447, and 441–447 bind to LC3s equally well. The Atg13 LIR in all three chimeric proteins were recognized by the same hydrophobic pockets of LC3, consisting of side-chains of Ile23, Lys49, Lys51, Phe52, Leu53, Ile66, and Phe108 via hydrophobic interactions to Phe444 of the Atg13 LIR (the W-site) and by main-chain hydrogen bonding between Lys51 and Leu53 of LC3 and Val445 and Ile446 of the Atg13 LIR (the L-site; Tables S1 and S2). A comparison with the binding interactions found in the previously reported crystal structure of the LC3B/p62 complex (Ichimura et al., 2008; PDB code 2ZJD) shows that the W/Y/FxxL/I/V motif, which in Atg13 is 444-FVMI-447 and in p62 is 340-WTHL-343, holds a similar conformation with similar interactions.

Lys49 Undergoes a Large Structural Rearrangement upon Atg13 LIR Binding

We then investigated side-chain structural arrangements by comparing the LC3A and Atg13-LC3A structures with sufficiently high resolutions, 2.00 Å and 1.77 Å, respectively. In the Atg13-LC3 isoform complex structures, the side-chains of Ile23, Lys49, Lys51, Phe52, Leu53, Ile66, and Phe108, and additionally in the Atg13-LC3A complex structure Glu19, His27, Lys30, and Pro55 of LC3, are involved in the interaction with $Atg13^{436–447}$ (Figure 5A). Upon $Atg13^{436–447}$ binding, these residues, except for Lys49, move slightly to reorganize (Figures 5A and 5B). In contrast, the side-chain of Lys49 in LC3A undergoes a large rotamer rearrangement. According to Wild et al. (2011), the Lys49 movement upon the optineurin LIR binding was also observed by the nuclear magnetic resonance experiment. In the uncomplexed structure, the gamma and epsilon carbon atoms of Lys49 form hydrophobic interactions with the aromatic ring of Phe52 (Figure 5C). However, in the complexed structure, the side-chain of Lys49 shifts by as much as 6.7 Å at the zeta nitrogen to open the hydrophobic interaction surface; as a result, both Phe52 and Lys49 form hydrophobic interactions with Val445 of Atg13 LIR.

Critical Residues for the Binding of Atg13 with LC3A

To determine the contribution of individual amino acid residues of Atg13 to the interaction with LC3, we measured relative binding abilities of point mutations in Atg13 compared with the wild-type (WT) protein using an SPR biosensor. The GST-fused Ala-substituted Atg13 LIR peptides were immobilized onto an SPR sensor chip via anti-GST antibodies (Figure 6A), and LC3A was injected onto the sensor chip. As shown in Figure 6B, the binding affinity to LC3A of all Ala-substituted mutants decreased significantly. In particular, the mutations of Phe444 (M4) and Ile447 (M7) to Ala reduced the binding affinity to ~25% (Figure 6B). The control protein (GST-GS) did not bind to LC3A.

Next, we investigated which residues in LC3A are required for Atg13 binding. In this experiment, we prepared six single mutations of LC3A to probe the LIR binding (Figure 6C). The first was

Please cite this article in press as: Suzuki et al., Structural Basis of the Autophagy-Related LC3/Atg13 LIR Complex: Recognition and Interaction Mechanism, Structure (2014), http://dx.doi.org/10.1016/j.str.2013.09.023

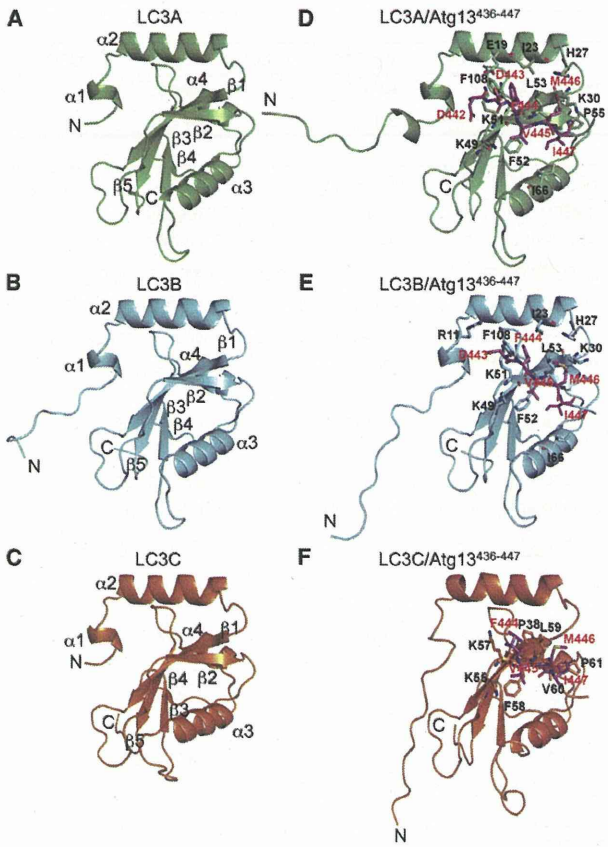

Figure 4. Overall Structures of Uncomplexed Form and Atg13 LIR-Fused LC3 Isoforms

Structures of uncomplexed form (A–C) and Atg13 LIR-fused LC3 isoforms (D–F) are represented by ribbon diagrams and colored in green (LC3A), cyan (LC3B), and orange (LC3C). LIR in symmetry-related molecules (magenta) and its interaction residues are shown in stick representation. Oxygen, nitrogen, and sulfur atoms are shown in red, blue, and yellow, respectively. The secondary structure was defined by the DSSP program (Kabsch and Sander, 1983).

E19D to investigate the LC3B binding. LC3B has significantly poorer binding to the Atg13 LIR compared with LC3A and LC3C (LC3A, 18.3 ± 0.6 μM; LC3B, 52 ± 7 μM; LC3C, 13 ± 6 μM), and Glu19 is the only binding residue that is conserved between LC3A and LC3C, but not LC3B (LC3A and LC3C, Glu; LC3B, Asp). Therefore, we predicted that a mutation at this site would have a significant effect on binding. The K49A and K49F mutations were designed to mimic the open and closed surface of LC3A, whereas the K51A, F52A, and L53A mutations were designed to probe the bottom floor of the binding site (Figure 5). $LC3A^{E19D}$ showed a slight increase in its binding ability to the Atg13 LIR (112 ± 2%). Interestingly, K49A mutation resulted in a marked increase 182 ± 2%, which presumably reflects the "always open" binding pocket formed by the methyl group of K49A. On the other hand, K51A and L53A mutations demonstrated reduced binding abilities (K51A, 29 ± 2%; L53A, 41 ± 1%, Figure 6D). Unfortunately, $LC3A^{K49F}$ and $LC3A^{F52A}$ aggregated on the sensor chip, increasing the resonance signals not only in Atg13 LIR immobilized flow cells but also in reference flow cells (data not shown), and the accurate binding abilities could not be estimated. The dissociation constants of K49A and K51A as the highest and the lowest binding ability mutants are measured by an SPR biosensor (Figure S5). The K_D values for $LC3A^{K49A}$ and $LC3A^{K51A}$ to GST-$Atg13^{411–447}$ were 6.6 ± 1.0 μM and 150 ± 2.6 μM, respectively. To verify the Atg13/LC3 interaction in vivo, we performed pulldown assay using HEK293 cells that expressed OSF-LC3A (WT, K49A, and K51A) and Myc-tagged ULK1 complex (Myc-ULK1, Myc-Atg101, Myc-FIP200, and Myc-Atg13) under nutrient-rich and starvation conditions (Figure S6). K49A mutant showed higher binding ability to the ULK1 complex than did WT; on the other hand, K51A mutation was similar or slightly decreased the binding ability to the ULK1 complex.

Movement of Lys49 Is Conserved in Mammalian LC3 Homologs

To investigate whether the side-chain configuration of Lys49 is conserved in LC3 homologs, we compared our LC3 structures with the eight reported LC3 homologs (Figure 7). The PDB contains four uncomplexed structures (ratLC3, 1UGM, Sugawara et al., 2004; GABARAP, 1KJT, Bavro et al., 2002; GATE-16, 1EO6, Paz et al., 2000; and Atg8, 2KWC, Kumeta et al., 2010) and four types of LIR-bound structures (LC3B/p62, 2ZJD, Ichimura et al., 2008; and 2K6Q, Noda et al., 2008; GABARAP/synthetic peptide, 3D32, Weiergräber et al., 2008; GABARAPL-1/NBR1, 2L8J, Rozenknop et al., 2011; and Atg8/Atg19, 2ZPN, Noda et al., 2008).

In the uncomplexed structures, except for Atg8, a yeast LC3 homolog, the side-chain carbon atoms of the equivalent Lys49 are located within 4 Å from the aromatic portion of Phe or Tyr at strand β2 (Lys49 and Phe52 in rat LC3 and Lys46 and Tyr49 in GATE-16, GABARAP, and Atg8 correspond to Lys49 and Phe52 in human LC3A). Thus, it seems that the residues corresponding to Lys49 of LC3A in the mammalian homologs cover the hydrophobic surfaces by interacting with these aromatic residues. In contrast, the side-chain of Lys46 in Atg8 faces away from Tyr49 and does not cover the interaction surface.

In the complexed structure of LC3B/p62, Lys49 does not interact with p62 LIR, although it undergoes a large structural rearrangement. In the GABARAP/synthetic peptide structure, the peptide forms an α-helix, instead of a parallel β sheet with strand β2 of GABARAP like other complex structures, and Lys46 moves only slightly upon peptide binding to break the hydrophobic interaction with Tyr49. Lys46 in the GABARAPL-1/NBR1 complex structure is oriented in the opposite direction to NBR1 LIR. The uncomplexed structure of GABARAPL-1 has not been reported; however, as mentioned above, the LIR interaction surface of GABARAP, which shares 87% identity with that of GABARAPL-1, is covered with a side-chain of Lys46. Taken together, these structural comparisons suggest that the movement of Lys49 side-chain is conserved in the mammalian LC3 proteins.

Lys49 Residue Plays Important Roles in Autophagosome Formation

To verify the importance of the interaction between Atg13 and the LC3 proteins in autophagosome formation, we established